Symmetry breaking induces room-temperature interface ferroelectricity in two-dimensional metastable mosaic-like heterostructures

Supplementary Information includes:

Supplementary Figures 1 to 26

Supplementary Tables 2

Supplementary Notes 2

Supplementary References

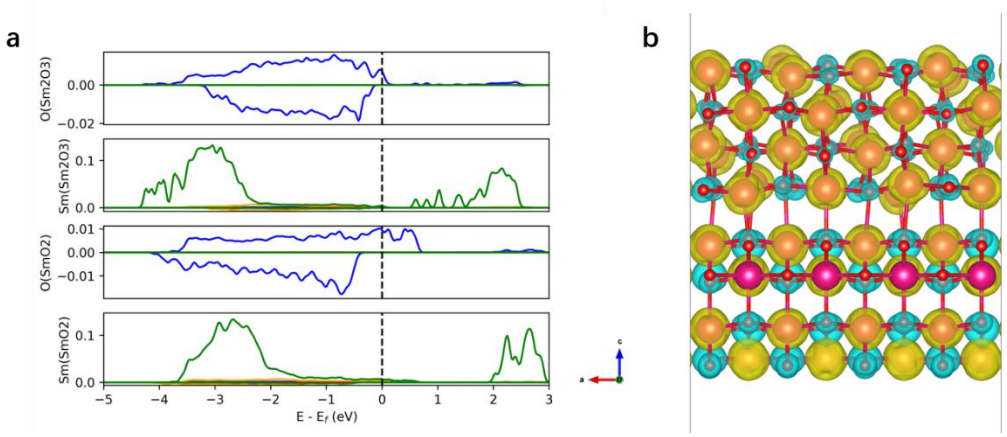

Supplementary Fig. 1 | Theory calculations of model. a, Calculated DOS of Sm_2O_3 and SmO_2 crystals. **b,** Calculated Spin-polarized charge distribution and atomic magnetic moment of heterostructure model.

For the Sm ions, the density of states below the Fermi level is dominated by the spin-up *f* orbitals, which indicates that the Sm ions are all in a spin-polarized state and their spin magnetic moments are primarily contributed by *f* electrons. In contrast, for the O ions, the density of states below the Fermi level is dominated by the O *p* orbitals. Furthermore, this asymmetry between the spin-up and spin-down *p* orbitals suggests that the magnetic moments of the O ions are mainly driven by spin polarization of the *p* orbitals.

The yellow surfaces correspond to spin-up polarization, while the blue surfaces correspond to spin-down polarization. Thus, electrons around the Sm ions exhibit predominantly spin-up polarization, whereas electrons around the oxygen ions exhibit predominantly spin-down polarization.

Quantitative analysis of these polarizations reveals distinct magnetic moments for different samarium oxides. For monoclinic SmO_2, the Sm ions exhibit an average magnetic moment of 5.0 μB, while the O ions contribute -0.44 μB. In comparison, cubic Sm_2O_3 shows a slightly higher average magnetic moment for Sm ions at 5.1 μB, and a reduced contribution from O ions at -0.11 μB. These quantitative magnetic moment values consistently reflect the described spin polarization trends, albeit with slight variations influenced by the specific crystalline structure.

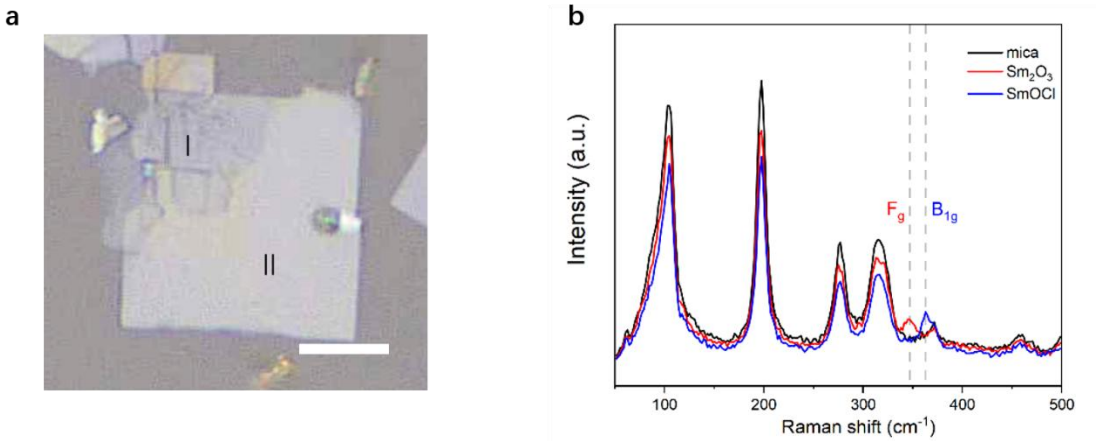

Supplementary Fig. 2 | Further oxidation phase transition. a, OM image of SmOCl and Sm_2O_3. Scale bars, 5 μm. **b**, Raman of SmOCl and Sm_2O_3.

Raman spectroscopic analysis of the optical image of the nanosheet reveals two distinct regions. Region I is assigned to Sm_2O_3, with a characteristic Raman peak at 343 cm^{-1} (F_g mode). Region II is assigned to SmOCl, with a characteristic Raman peak at 361 cm^{-1} (B_{1g} mode). The coexistenceof Sm_2O_3 and SmOCl suggests that SmOCl undergoes further oxidation to Sm_2O_3 during the growth process.

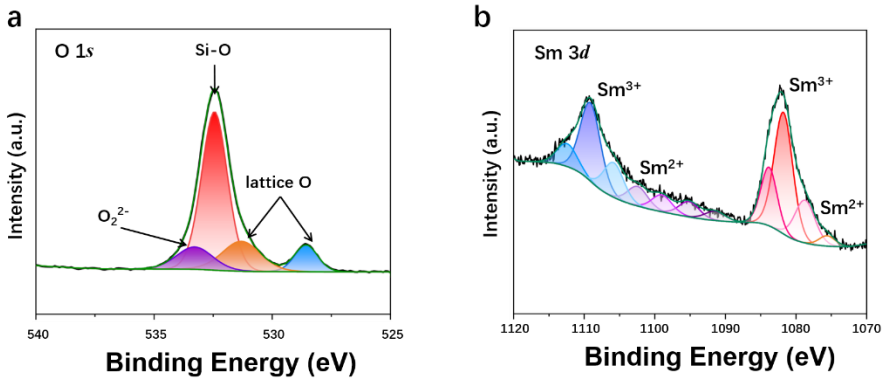

Supplementary Fig. 3 | XPS characterization. a, XPS spectra of O 1*s*. **b,** XPS spectra of Sm 3*d*.

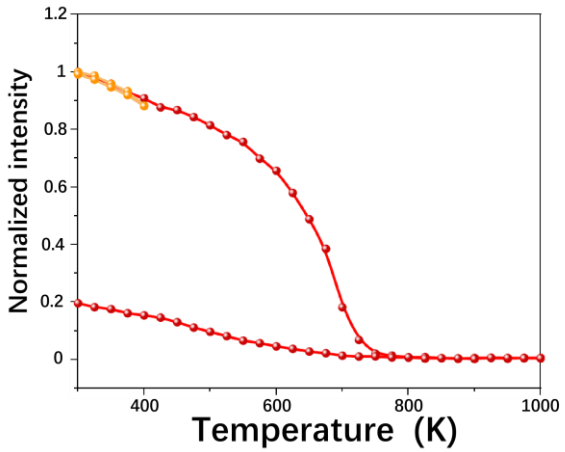

Supplementary Fig. 4 | Temperature-dependent SHG intensity during heating-cooling cycles.

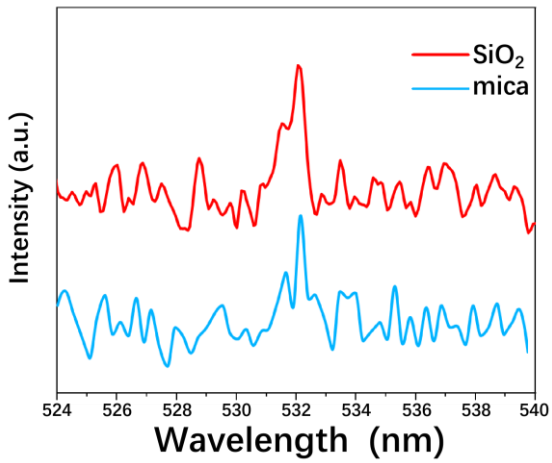

Supplementary Fig. 5 | SHG signal of the nanosheets on the diffferent substrates.

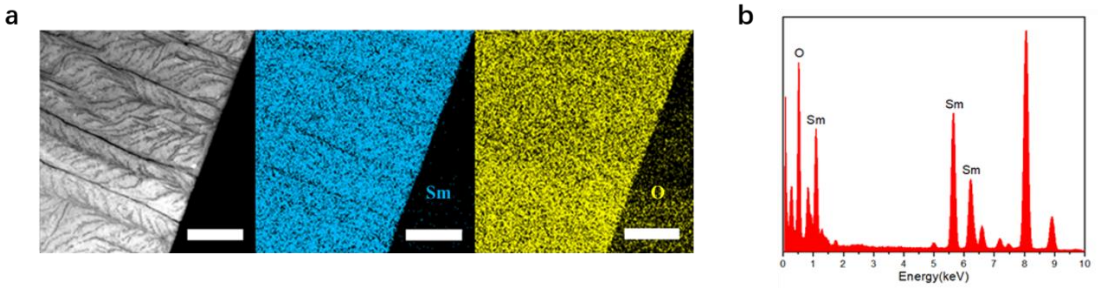

Supplementary Fig. 6 | Elemental analysis of samarium oxide nanosheets. a, EDS mapping. Scale bars, 2 μm. **b**, EDS spectrum.

Elemental analysis demonstrates a uniform distribution of Sm and O throughout the nanosheets. Notably, the TEM-EDS spectrum of the nanosheets confirmed the absence of Fe elements in the final product.

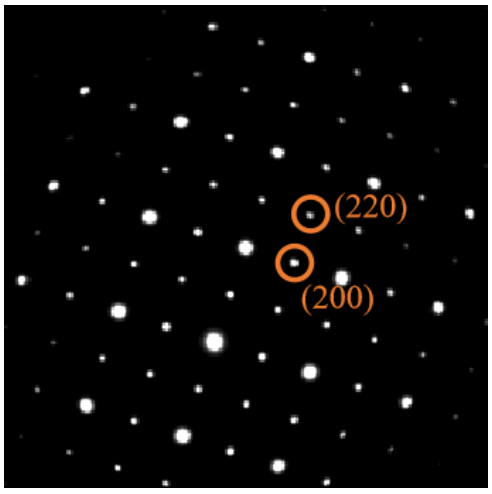

Supplementary Fig. 7 | Selected area electron diffraction (SAED) imge of Sm_2O_3.

Thin nanosheets along the [001] axis shows a single set of rectangular diffraction spots indicative of a high-quality single-crystalline structure. The circled bright spots can be assigned to (200) and (220), confirming its 4-fold symmetric structure.

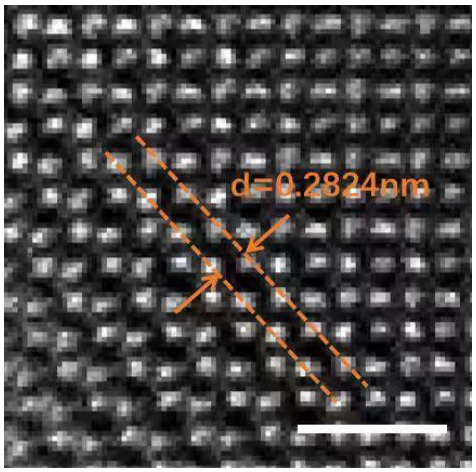

Supplementary Fig. 8 | High-magnification HAADF-STEM image of the interface of SmO_2/Sm_2O_3 heterostructure. Scale bars, 1 nm. The interlayer distance of interface was found to be 0.2824 nm.

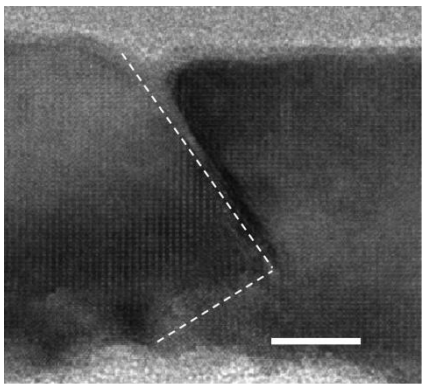

Supplementary Fig. 9 | Cross-section TEM image of SmO_2/Sm_2O_3 heterostructure. Scale bar, 20nm

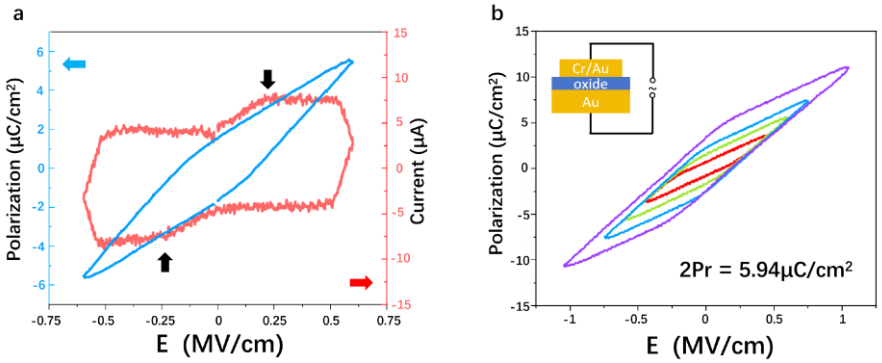

Supplementary Fig. 10 | Macroscopic ferroelectric measurements a, Polarization and current versus electric field for the SmO_2/Sm_2O_3. **b**, Polarization measured under increasing maximum electric field.

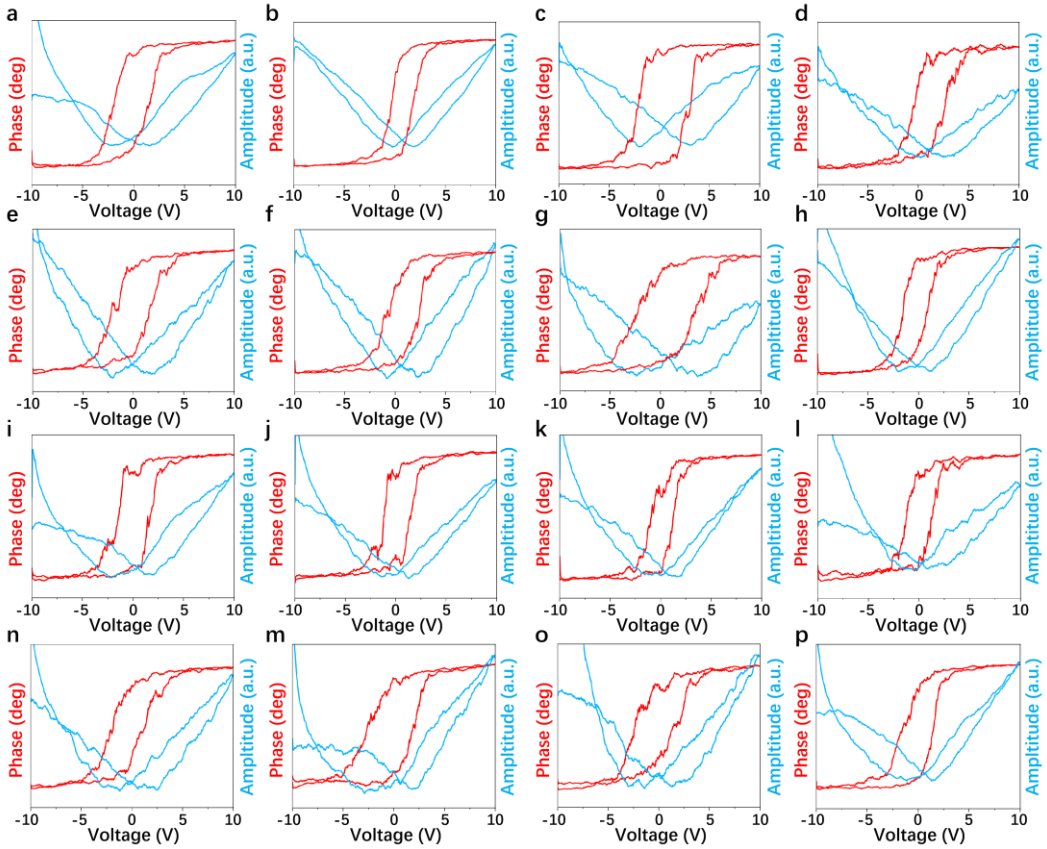

Supplementary Fig. 11 | PFM characteristic of multiple flakes.

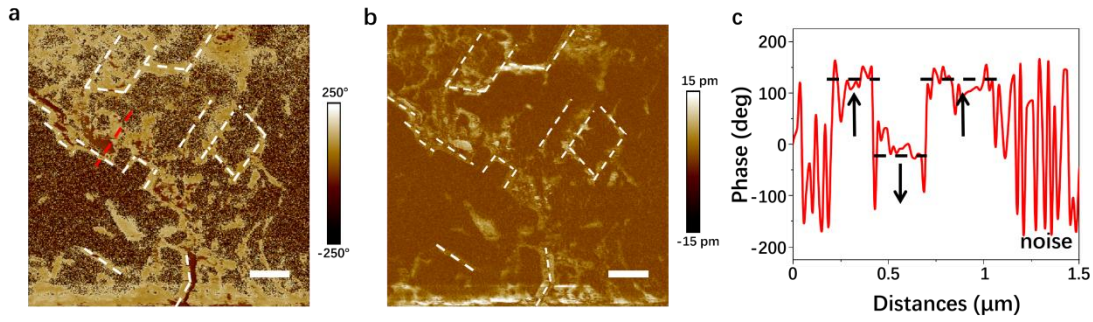

Supplementary Fig. 12 | Phase characterization a, PFM phase image. Scale bar, 1μm. **b**, PFM amplitude image. Scale bar, 1μm. **c** The PFM phase profile along the red dasn line shown in a.

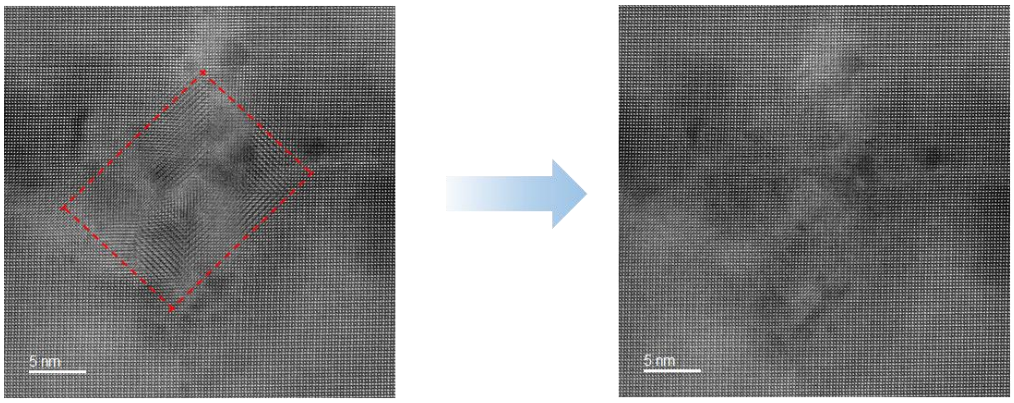

Supplementary Fig. 13 | TEM image of atomic structure. Under electron-beam irradiation during TEM, the metastable SmO_2 phase gradually transforms into the more stable Sm_2O_3. The SmO_2 is preferentially oriented and embedded within the Sm_2O_3 matrix, thereby constituting a mosaic-like lateral heterostructure.

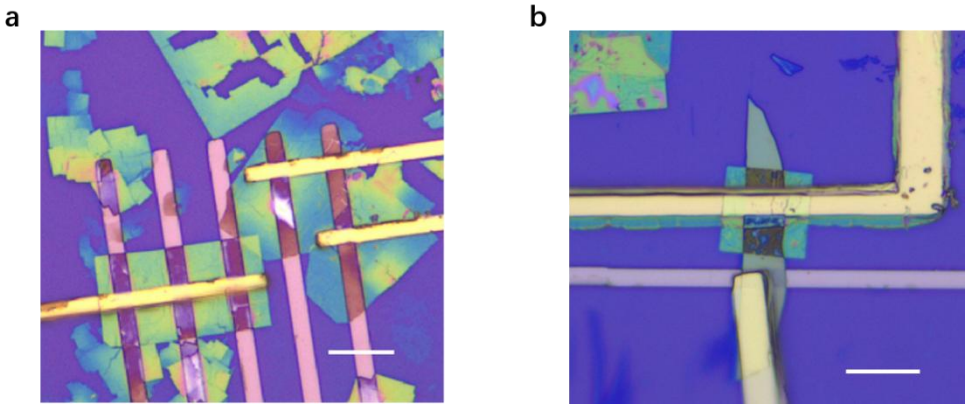

Supplementary Fig. 14 | OM image of memristors. a, Ti/SmO_2/Sm_2O_3/Au. Scale bars, 5 μm. **b,** Ti/SmO_2/Sm_2O_3/Gr. Scale bars, 5 μm

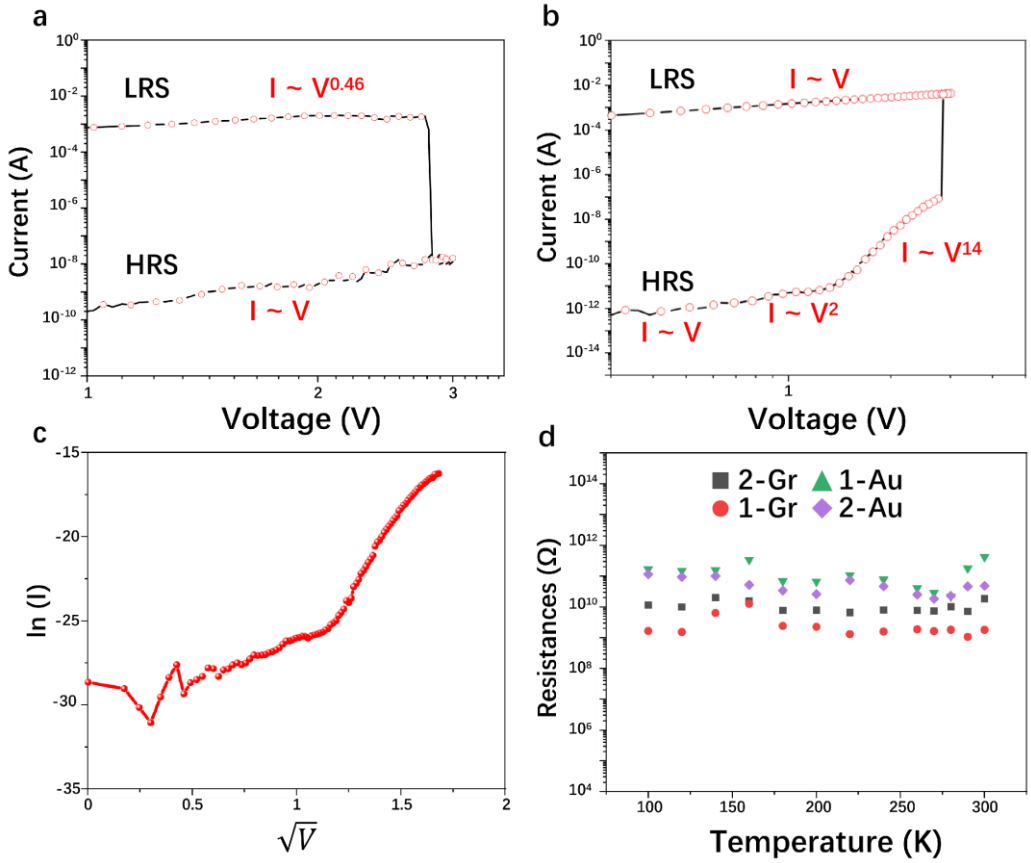

Supplementary Fig. 15 | Transport mechanism analysis of the Ti/SmO_2/Sm_2O_3 memristor with Au and Gr bottom electrodes. a and **b,** *I-V* characteristics of Ti/SmO_2/Sm_2O_3/Gr and Ti/SmO_2/Sm_2O_3/Au during the RESET operation. **c,** The ln(*I*) versus*V* for the Au-device in the HRS. **d,** Temperature-dependent resistance of the Gr- and Au-devices in HRS measured from 300 K to 100 K.

The *I-V* characteristics of Gr-bottom-electrode device is shown in Fig. S15a. As a semimetal, graphene possesses conduction and valence bands that meet at the Dirac point, exhibiting a linear dispersion relation rather than the parabolic dispersion characteristic of conventional metals[1]. This electronic structure allows the Fermi level of graphene to be modulated via external stimuli, such as electric fields or chemical doping. Unlike conventional metal electrodes, electron transfer between graphene and semiconductors mitigates pinning, enabling the Fermi level of graphene to align naturally with the semiconductor, thereby eliminating the potential barrier[2]. Consequently, the experiment observed Ohmic contact behavior in the HRS. Furthermore, the heterogeneous electron transfer (HET) dynamics are determined not only by the driving force (potential difference) but also by electronic coupling[3]. Electronic coupling reflects the probability of electron tunneling across the interface and stems from the density of states (DOS) of the electrode material. In contrast, upon switching to the LRS where oxygen vacancy conductive filaments penetrate the interface, localized states on the graphene surface introduce intermediate energy levels and modulate the interface barrier. These modifications cause the electron injection efficiency to vary non-linearly with voltage, leading to the sublinear transport characteristic of $I \sim V^{0.46}$ observed experimentally. This sublinear transport characteristic serves as a macroscopic manifestation of HET kinetics being modulated by localized defect states.

Conversely, for the Au-electrode devices (Fig. S15b), the double-logarithmic *I-V* plot reveals a clear three-regime behavior: an Ohmic region (n ≈ 1) at low voltages, a Child's law region (n ≈ 2) at intermediate voltages, and a trap-filled limit (TFL) region with a steep exponent of n ≈ 14 at high voltages. This sequential transition is characteristic of space-charge-limited conduction (SCLC) mediated by an exponential distribution of bulk traps[4]. The high exponent in the TFL region is suggestive of rapid filling of deep-level traps by injected carriers, leading to a sudden current surge once all traps are occupied. Crucially, temperature-dependent resistance measurements for the Au-electrode devices (Fig. S15d) conducted from 300K down to 100 K show negligible variation in the HRS. This weak temperature dependence, combined with the absence of a linear regime in the ln(*I*) versus *V* plot across the entire voltage range, does not support thermally activated processes such as Schottky or Poole-Frenkel emission, and is more compatible with defect-mediated tunneling transport[5]. While we acknowledge that the transport analysis alone does not uniquely prove the switching mechanism, these observations are consistent with the presence of a high density of oxygen vacancies, which are the likely candidate defects responsible for the valence-change switching[6].

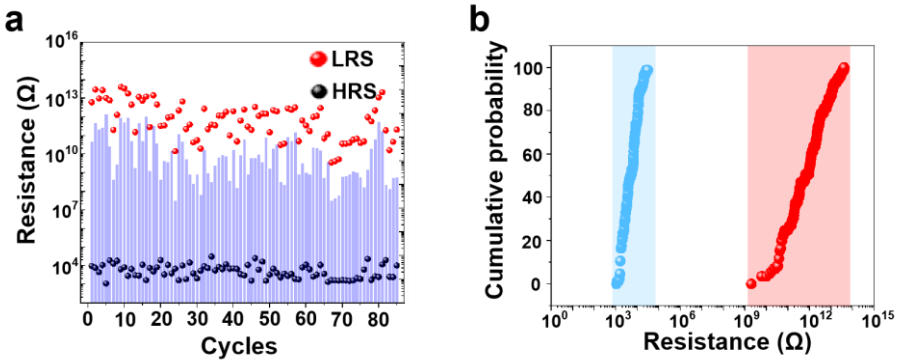

Supplementary Fig. 16 | Statistical distribution of HRS and LRS during 85 cycles for Gr-based device(CC = 50μA). a, High/low resistance states (H/LRS) and switch ratio of Au/Ti/SmO_2/Sm_2O_3/Gr memristor under 85 cycles(CC= 50μA). **b,** Cumulative probability of the resistance levels at the LRS and HRS(CC= 50μA).

Supplementary Note 1: Thermal Stability Assessment of the Conductive Filament During Device Operation

The I-V characteristics were measured with a 1μA compliance current to prevent excessive heating and a slow voltage sweep to ensure quasi-steady-state conditions. To preliminarily estimate the operating temperature of the device, a simplified thermal model was constructed based on the vertical structure, where the oxygen-vacancy conductive filament is approximated as a cylindrical channel bridging the two electrodes. Under these quasi-steady-state conditions, the filament temperature is derived from the following equations:

$$P = I \times V \quad (1)$$

$$T = T_0 + \frac{P}{R_{th}} \quad (2)$$

$$R_{th} = \frac{d}{k_{th} \times A} \quad (3)$$

where P is the Joule heating power, I and V are the measured current and voltage respectively, T0 is the ambient temperature of 300K, d is the oxide thickness (filament length, 35nm), R_{th} is the thermal resistance, k_{th} is the thermal conductivity, and $A = \pi r^2$ represents the filament horizontal cross-section area, r denotes the filament radius which is estimated from the current distribution measured by C-AFM, giving $r \approx 25$nm.

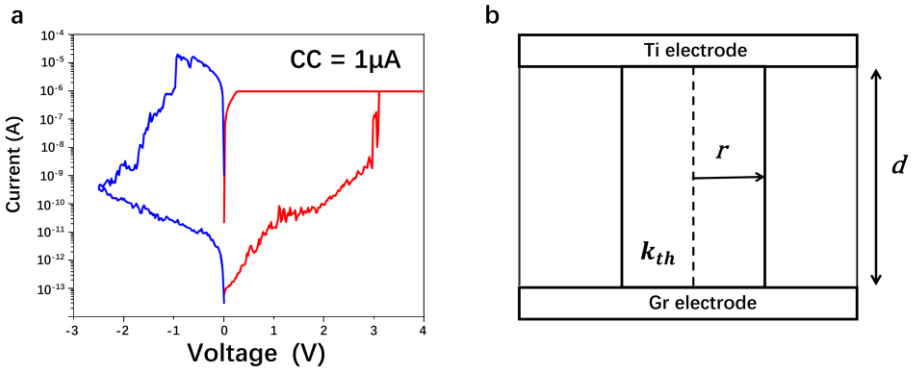

Supplementary Fig. 17 | Thermal Stability Assessment During Device Operation a, *I-V* switching curve of a Ti/SmO_2/Sm_2O_3/Gr memristor at compliance current(CC) = 1μA. **b,** Schematic diagram of one-dimensional simplified thermal model for memristor.

The thermal conductivity of epitaxially grown single-crystalline rare-earth oxide films is approximately five times that of SiO_2[7]. Given a SiO_2 thermal conductivity of ~ 1.3W/m·K[8] the conductivity is estimated at ~ 6.5 W/m·K. However, in oxygen-vacancy-rich filaments, high defect concentrations induce strong phonon scattering. According to the Klemens model and prior simulations on oxide memristor filaments[9], the local thermal conductivity in such regions can decrease by at least one order of magnitude relative to the pristine lattice. To ensure a rigorous assessment, we adopt a thermal conductivity of k_{th} = 0.65 W/m·K as a reasonable baseline for the filament region. Regarding the power parameters used in the model, although the maximum RESET power extracted from the measured I-V cycles is ~ 1.89μW, we utilize a value of $P \approx 10$μW to accout for device-to-device variations.

The peak filament temperature is estimated at 574 K, representing a conservative upper bound for the actual operating temperature because the one-dimensional model neglects radial heat loss

and electrode heat-sink effects. Serving as a qualitative assessment rather than an exact measurement, this estimate aims to determine whether thermal effects could trigger irreversible phase transformations. Under these assumptions, the conclusion that the peak temperature remains below the phase-transition threshold remians credible, suggesting the potential for thermally stable device operation under low-compliance-current measurement conditions.We have added the relevant content to the supplementary information.

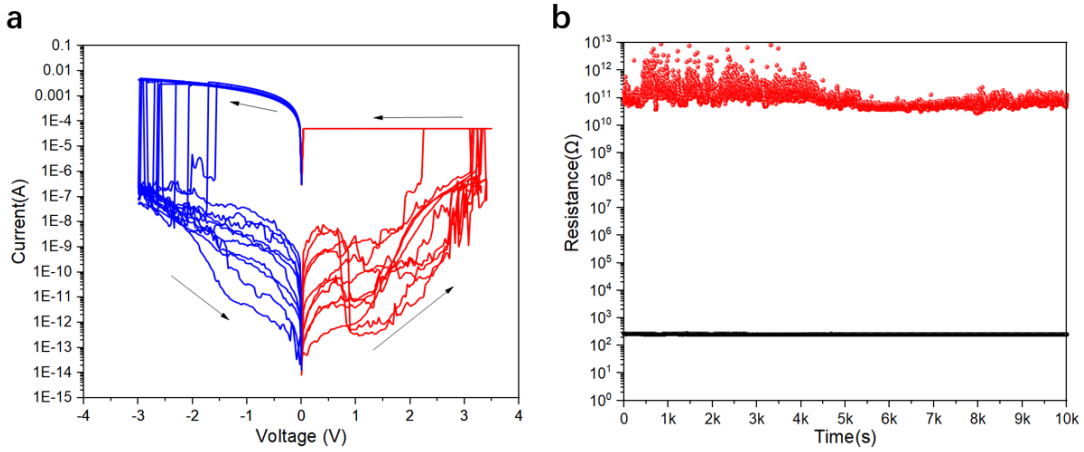

Supplementary Fig. 18 | Electrical characteristics of the Ti/Sm_2O_3/Au. a, *I–V* switching curves of a Ti/SmO_2/Sm_2O_3/Au memristor. **b,** Retention time characteristic of Ti/SmO_2/Sm_2O_3/Au memristor.

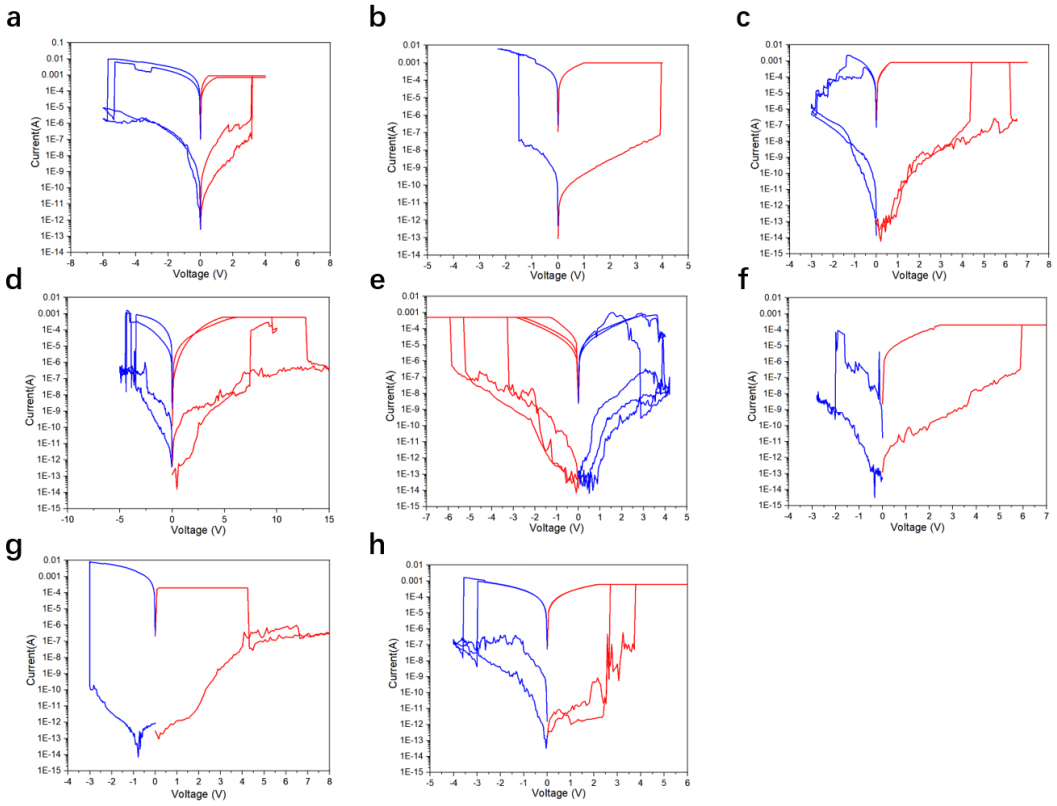

Supplementary Fig. 19 | *I-V* characteristics of multiple Ti/SmO_2/Sm_2O_3/Au memristors.

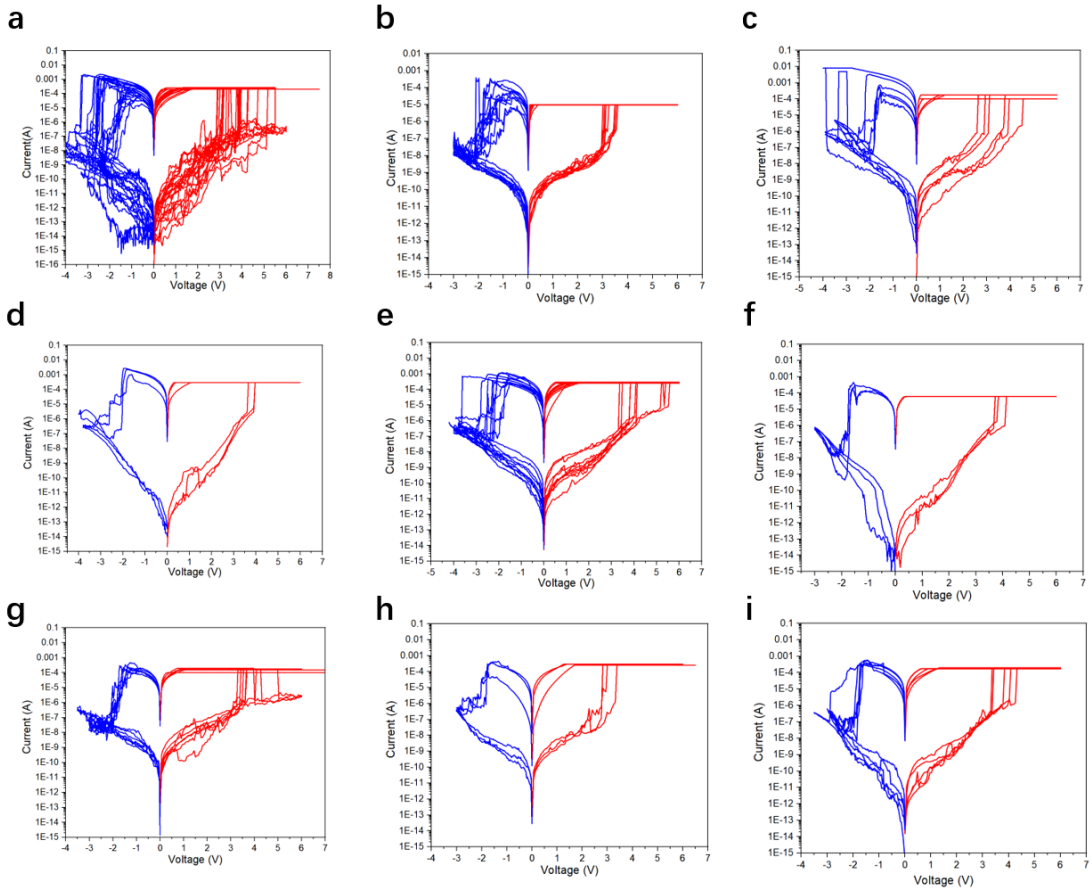

Supplementary Fig. 20 | *I-V* characteristics of multiple Ti/SmO_2/Sm_2O_3/Gr memristors.

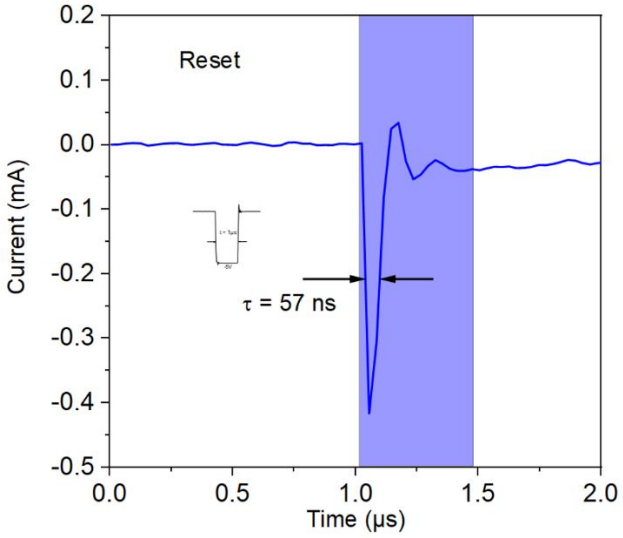

Supplementary Fig. 21 | Reset behavior of Ti/SmO_2/Sm_2O_3/Gr memristor at -5V(1μs) pulse. The current response confirming a transition to HRS, shows the highest speed with a switching time of 57 ns.

Table S1 Comparison of on/off ratio and switching time with various devices

No.	Device	on/off ratio	Switching time	Reference
1	F-doped TiO_{2-x}	$>10^4$	77.7 ns	[10]
2	(MTS)h-BN/HfO_2	~100	4.2 ns	[11]
3	Gr/$MoS_{2-x}O_x$/Gr	12	<100 ns	[12]
4	h-BN	$\sim10^3$	680 ns	[13]
5	Ti/h-BN/Au	50	120 ps	[14]
6	MoS_2	$\sim10^6$	330 ps	[15]
7	Ti/SiN_x/p+Si	~10	500 ns	[16]
8	Ag/TiO_2/Pt	$\sim10^3$	20 ns	[17]
9	Ta/Ta_2O_5/AlN/Gr	~100	50 ns	[18]
10	Pd/SiO_x/Gr	$>10^6$	35 ns	[19]
11	Ta/HfO_2/Pt	>10	5 ns	[20]
12	Pt/HfO_2/Pt	$\sim10^6$	120 ns	[21]
13	Ti/$HfSe_xO_y$/$HfSe_2$ /Au	$\sim10^3$	<50 ns	[22]
14	Ti/$PdSe_2$/Au	$\sim10^3$	50 ns	[23]
15	Ti/SmO_2/Sm_2O_3/Gr	$>10^9$	47.3 ns	This work

Table S2 Comparison of on/off ratio with various samarium oxide-based memristors

Device	Synthesis method	on/off ratio	retention time(s)	year	reference
Pt//Sm_2O_3/TiN	RF magnetron sputtering	$10^{2.2}$	10^4	2011	[24]
Pt//Sm_2O_3/TiN	RF magnetron sputtering	$10^{2.5}$	10^4	2011	[25]
Ru/SmO_x/TaN	RF magnetron sputtering	10^3	10^5	2012	[26]
Ni/Sm_2O_3/ITO	RF magnetron sputtering	10^2	10^5	2013	[27]
Ni//Sm_2O_3/ITO	RF magnetron sputtering	10^2	10^5	2014	[28]
Pt/V_2O_5//Sm_2O_3/TiN/SiO_2/Si	RF magnetron sputtering	10^2	-	2018	[29]
Al/V_2O_5//Sm_2O_3/TiN/SiO_2/Si	RF magnetron sputtering	10^3	10^4	2019	[30]
Ag/Sm_2O_3/Pt	-	10^4	10^4	2019	[31]
Ti/SmO_2/Sm_2O_3/Gr	Eutectic Salt-Assisted	$>10^9$	10^4	2026	This work

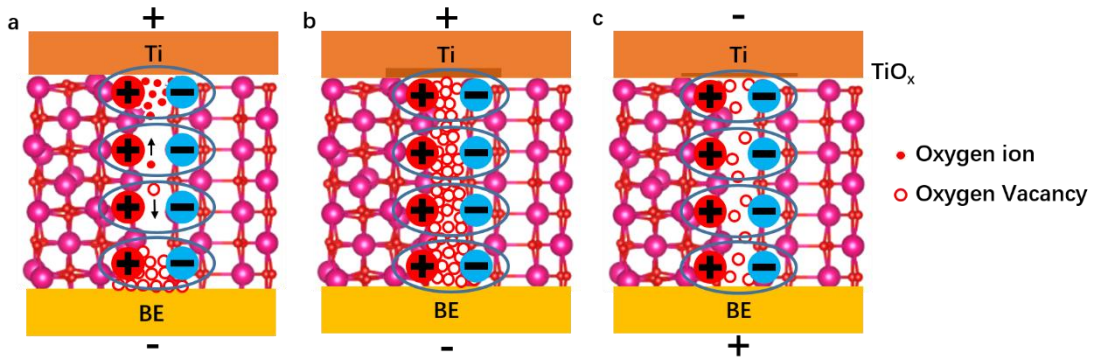

Supplementary Fig. 22 | Schematic of the resistive switching mechanism.

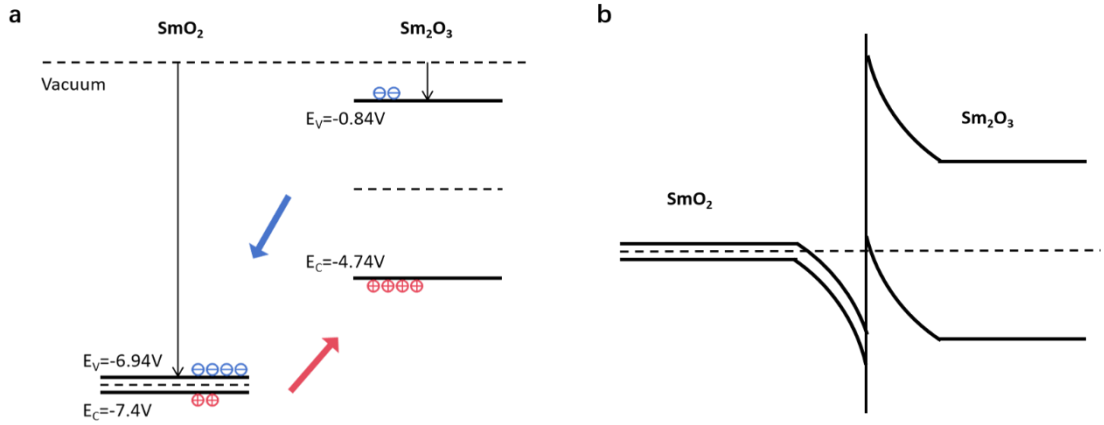

Supplementary Fig. 23 | Calculated band structure of Sm_2O_3 and SmO_2 crystals. a, Energy band and carrier injection of SmO_2 and Sm_2O_3 crystals. **b,** Energy band diagram near the interface of SmO_2/Sm_2O_3 heterostructure.

Upon contact between Sm_2O_3 and SmO_2, charge redistribution occurs to equalize their Fermi levels. This process involves the transfer of electrons from Sm_2O_3 into SmO_2, driven by the energetically favorable alignment where the conduction band minimum of SmO_2 lies approximately 2.2 eV lower than the valence band maximum of Sm_2O_3. Consequently, the difference in Fermi levels between SmO_2 and Sm_2O_3 leads to charge transfer, where holes transfer from SmO_2 to Sm_2O_3 and electrons transfer from Sm_2O_3 to SmO_2 respectively. This process consequently induces downward energy band bending at the SmO_2 interface and upward bending at the Sm_2O_3 interface.

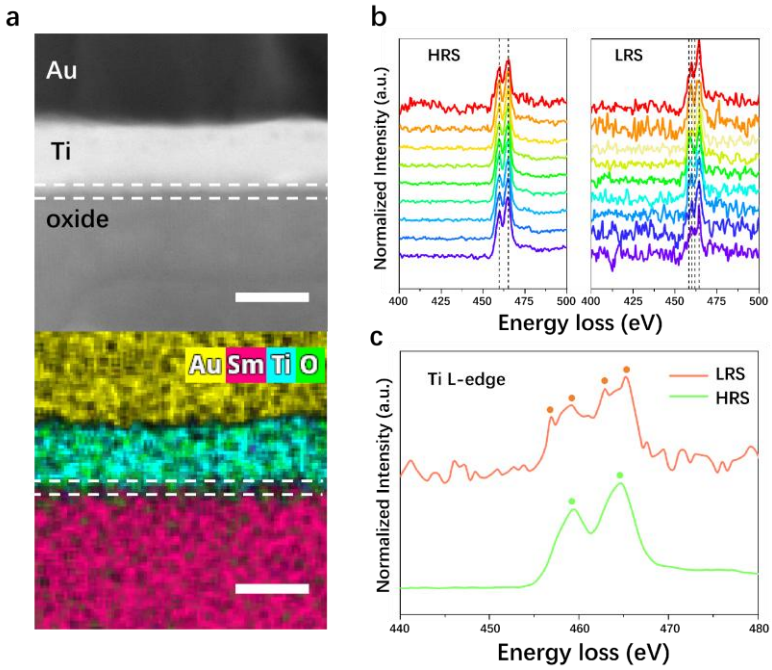

Supplementary Fig. 24 | Cross-sectional TEM-EELS chemical analysis of Ti at the electrode interface in HRS and LRS. a, TEM image and EDS mapping of the interface. Scale bar, 10nm. **b**,Ti L-edge EEL spectra as a function of position for the device in the HRS and LRS. The spectra were acquired across the Ti electrode from the bottom to the top. **c**, Comparison of Ti L-edge EEL spectra between HRS and LRS. (c) O K-edge normalized intensity for the same region in the HRS and LRS.

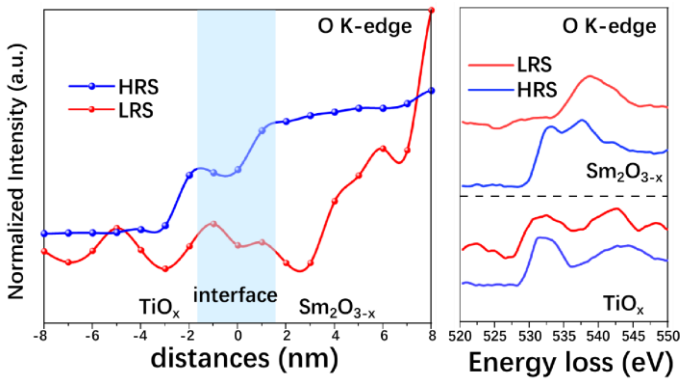

Supplementary Fig. 25 | Cross-sectional TEM-EELS chemical analysis of O at the electrode interface in HRS and LRS

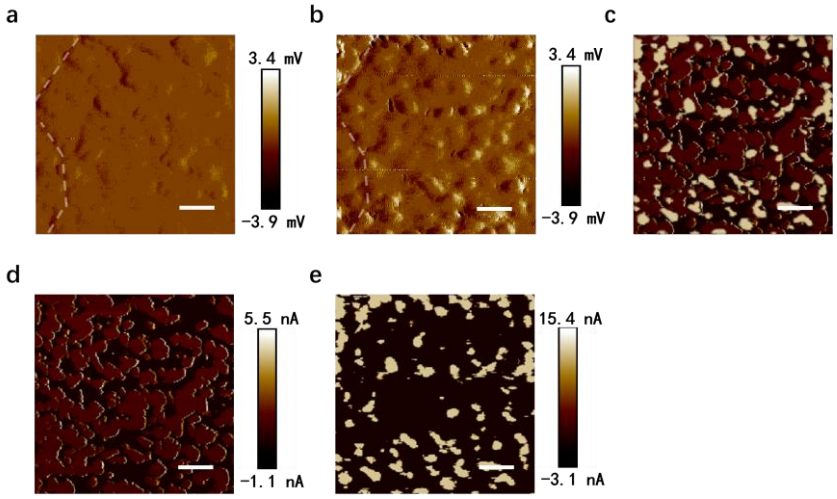

Supplementary Fig. 26 | C-AFM characterization of the memristive device in HRS and LRS. **a**, The C-AFM surface deflection at HRS. **b**, The C-AFM surface deflection acquired immediately after the forming process. **c**, Spatially superimposed C-AFM current maps acquired from the same device region in the HRS and LRS. **d**, The C-AFM current mapping images of device at HRS. **e**, The C-AFM current mapping images of device at LRS. All scale bar, 200nm.

Supplementary Note 2: Computational details

The calculations of density functional theory are done with the projector augmented plane-wave basis, which is implemented in Vienna *ab-initio* simulation package[32]. And the plane-waves are cut-off at 550 eV. The exchange-correlations of electrons are described by the generalized gradient approximations with the form proposed by Perdew, Burke, and Ernzerhof[33]. The 4f electrons of Sm were treated as part of the ionic core. Vacuum layer of 20 Å is set in *z*-direction which is supposed to be nonperiodic to eliminate the interactions between images. Dipole correction is considered. The energy converge criterion for solving self-consistent Kohn-Sham equations is 10^{-7} eV. The Brillouin zone is sampled with resolutions better than 0.03 $Å^{-1}$, using the scheme of Monkhorst-Pack[34]. All the structures in this study are fully relaxed until the Hellman-Feynman smaller than 0.05 eV/Å.

Reference

1. Zhou SY, Gweon GH, Graf J, Fedorov AV, Spataru CD, Diehl RD, et al. First direct observation of Dirac fermions in graphite. Nature Physics 2006, 2(9): 595-599.
2. Hong S, Hong C-U, Lee S, Jang M, Jang C, Lee Y, et al. Ultrafast van der Waals diode using graphene quantum capacitance and Fermi-level depinning. Science Advances 2023, 9(29): eadh9770.
3. Maroo S, Coello Escalante L, Wang Y, Erodici MP, Nessralla JN, Tabo A, et al. Electronic origin

of reorganization energy in interfacial electron transfer. Nature 2026, 653(8113): 98-103.

4. Wright GT. Space-Charge Limited Currents in Insulating Materials. *Nature* 1985, **182**(4645): 1296-1297.
5. Park J, Kumar A, Zhou Y, Oh S, Kim J-H, Shi Y, *et al*. Multi-level, forming and filament free, bulk switching trilayer RRAM for neuromorphic computing at the edge. *Nat. Commun.* 2024, **15**(1): 3492.
6. Wedig A, Luebben M, Cho D-Y, Moors M, Skaja K, Rana V, *et al*. Nanoscale cation motion in TaO_x, HfO_x and TiO_x memristive systems. *Nat. Nano.* 2016 **11**(1): 67-74.
7. Dargis R, Williams D, Smith R, Arkun E, Semans S, Vosters G, *et al*. Study of the Structural and Thermal Properties of Single Crystalline Epitaxial Rare-Earth-Metal Oxide Layers Grown on Si(111). *ECS Trans.* 2011, **41**(3): 161
8. Pei Y, Chen L, Jeon W, Liu Z, Chen R. Low-dimensional heat conduction in surface phonon polariton waveguide. *Nat. Commun.* 2023 **14**(1): 8242
9. Gurunathan R, Hanus R, Snyder GJ. Alloy scattering of phonons. *Mater. Horiz.* 2020, **7**(6): 1452-1456.
10. Bae J, Kwon C, Park S-O, Jeong H, Park T, Jang T*, et al.* Tunable ion energy barrier modulation through aliovalent halide doping for reliable and dynamic memristive neuromorphic systems. *Science Advances* 2024, **10**(23)**:** eadm7221.
11. Dang W, Shen Y, Wei W, Pan C, Chen F, Ruan G-J*, et al.* Mortise-tenon–shaped memristors for scientific computing. *Science Advances* 2025, **11**(18)**:** eadu3309.
12. Wang M, Cai S, Pan C, Wang C, Lian X, Zhuo Y*, et al.* Robust memristors based on layered two-dimensional materials. *Nature Electronics* 2018, **1**(2)**:** 130-136.
13. Zhu K, Pazos S, Aguirre F, Shen Y, Yuan Y, Zheng W*, et al.* Hybrid 2D–CMOS microchips for memristive applications. *Nature* 2023, **618**(7963)**:** 57-62.
14. Teja Nibhanupudi SS, Roy A, Veksler D, Coupin M, Matthews KC, Disiena M*, et al.* Ultra-fast switching memristors based on two-dimensional materials. *Nature Communications* 2024, **15**(1)**:** 2334.
15. Kim M, Ducournau G, Skrzypczak S, Yang SJ, Szriftgiser P, Wainstein N*, et al.* Monolayer molybdenum disulfide switches for 6G communication systems. *Nature Electronics* 2022, **5**(6)**:** 367-373.
16. Kim S, Jung S, Kim M-H, Chen Y-C, Chang Y-F, Ryoo K-C*, et al.* Scaling Effect on Silicon Nitride Memristor with Highly Doped Si Substrate. *Small* 2018, **14**(19)**:** 1704062.
17. Sahu MC, Jena AK, Mallik SK, Roy S, Sahoo S, Ajimsha RS*, et al.* Reconfigurable Low-Power TiO_2 Memristor for Integration of Artificial Synapse and Nociceptor. *ACS Applied Materials & Interfaces* 2023, **15**(21)**:** 25713-25725.
18. Yan X, Cao G, Wang J, Man M, Zhao J, Zhou Z*, et al.* Memristors based on multilayer graphene electrodes for implementing a low-power neuromorphic electronic synapse. *Journal of Materials Chemistry C* 2020, **8**(14)**:** 4926-4933.
19. Choi S, Choi J-W, Kim JC, Jeong HY, Shin J, Jang S*, et al.* Energy-efficient three-terminal SiOx memristor crossbar array enabled by vertical Si/graphene heterojunction barristor. *Nano Energy* 2021, **84:** 105947.
20. Jiang H, Han L, Lin P, Wang Z, Jang MH, Wu Q*, et al.* Sub-10 nm Ta Channel Responsible for Superior Performance of a HfO_2 Memristor. *Scientific Reports* 2016, **6**(1)**:** 28525.
21. Zhang Y, Mao G-Q, Zhao X, Li Y, Zhang M, Wu Z*, et al.* Evolution of the conductive filament

system in HfO_2-based memristors observed by direct atomic-scale imaging. *Nature Communications* 2021, **12**(1)**:** 7232.

22. Liu L, Li Y, Huang X, Chen J, Yang Z, Xue K-H*, et al.* Low-Power Memristive Logic Device Enabled by Controllable Oxidation of 2D $HfSe_2$ for In-Memory Computing. *Advanced Science* 2021, **8**(15)**:** 2005038.
23. Li Y, Loh L, Li S, Chen L, Li B, Bosman M*, et al.* Anomalous resistive switching in memristors based on two-dimensional palladium diselenide using heterophase grain boundaries. *Nature Electronics* 2021, **4**(5)**:** 348-356.
24. Huang SY, Chang TC, Chen MC, Sze SM, Tsai MJ. Investigation of resistive switching properties in Sm_2O_3 memory devices. 2011 11th Annual Non-Volatile Memory Technology Symposium Proceeding; 2011 7-9 Nov. 2011; 2011. p. 1-3.
25. Huang S-Y, Chang T-C, Chen M-C, Chen S-C, Lo H-P, Huang H-C*, et al.* Resistive switching characteristics of Sm_2O_3 thin films for nonvolatile memory applications. *Solid-State Electronics* 2011, **63**(1)**:** 189-191.
26. Pan TM, Lu CH. Switching Behavior in Rare-Earth Films Fabricated in Full Room Temperature. *IEEE Transactions on Electron Devices* 2012, **59**(4)**:** 956-961.
27. Mondal S, Chueh CH, Pan TM. High-Performance Flexible Ni/Sm_2O_3/ITO ReRAM Device for Low-Power Nonvolatile Memory Applications. *IEEE Electron Device Letters* 2013, **34**(9)**:** 1145-1147.
28. Mondal S, Chueh C-H, Pan T-M. Current conduction and resistive switching characteristics of Sm_2O_3 and Lu_2O_3 thin films for low-power flexible memory applications. *Journal of Applied Physics* 2014, **115**(1).
29. Jian-Yang Lin K-YW, Kai-Huang Chen, Chien-Min Cheng, and Cheng-Ying Li. Bipolar Switching Properties of Bilayer V_2O_5/Sm_2O_3 Thin-film Resistive Random Access Memory Device Prepared by Sputtering Technology. *Sensors and Materials* 2018, **30**(4)**:** 933-938.
30. Lin J-Y, Wu K-Y, Chen K-H. Effects of Sm_2O_3 and V_2O_5 Film Stacking on Switching Behaviors of Resistive Random Access Memories. *Crystals* 2019, **9**(6)**:** 318.
31. Ji M, Wu Y, Zhang Z, Wang Y, Liu H. Bipolar resistive switching characteristics of samarium oxide solid electrolyte thin films for non-volatile memory applications. *Functional Materials Letters* 2019, **12**(03)**:** 1950023.
32. Kresse G, Joubert D. From ultrasoft pseudopotentials to the projector augmented-wave method. *Physical Review B* 1999, **59**(1758).
33. Perdew JP, Burke K, Ernzerhof M. Generalized Gradient Approximation Made Simple. *Physical Review Letters* 1996, **77**(18)**:** 4.
34. Monkhorst HJ, Pack JD. Special points for Brillouin-zone integrations. *Physical Review B* 1976, **13**(12)**:** 5.